Journal of Power Sources 536 (2022) 231491

Contents lists available at ScienceDirect

Journal of Power Sources

journal homepage: www.elsevier.com/locate/jpowsour

Improving the stability of NASICON-type electrolyte with Li metal anode by interfacial modification

Can Huang [a], Zhuojie Li [b], Shanshan Duan [a], Shuhong Xie [b], Shuoguo Yuan [a,**], Shuen Hou [a], Guozhong Cao [c], Hongyun Jin [a,*]

[a] Engineering Research Center of Nano-Geo Materials of Ministry of Education, Faculty of Materials Science and Chemistry, China University of Geosciences, Wuhan, 430074, China

[b] Key Laboratory of Low Dimensional Materials and Application Technology of Ministry of Education, School of Materials Science and Engineering, Xiangtan University, Xiangtan, 411105, China

[c] Department of Materials Science and Engineering, University of Washington, WA, 98195, USA

HIGHLIGHTS

- LATP is modified by a MoS_2 coating layer via spin coating method.
- The MoS_2 coating layer suppresses the decomposition of LATP.
- The MoS_2 coating layer improves the interfacial charge kinetics.
- The modified batteries cycle over 300 cycles at 1C.

GRAPHICAL ABSTRACT

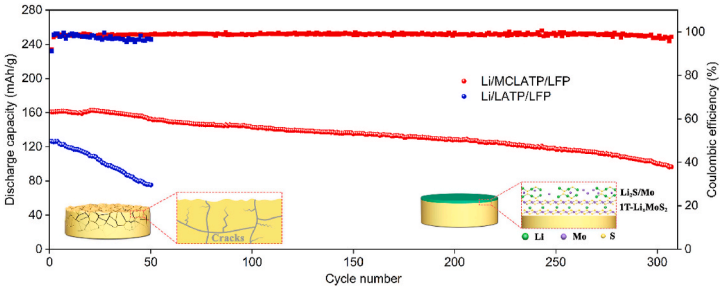

ARTICLE INFO

Keywords:
NASICON
LATP
MoS_2
Artificial SEI
Lithium metal batteries

ABSTRACT

Sodium super-ionic conductors (NASICON)-type electrolyte $Li_{1.4}Al_{0.4}Ti_{1.6}(PO_4)_3$ (LATP), with high ionic conductivity and low cost, is considered as one of the most attractive alternatives to liquid electrolytes. However, the poor interfacial compatibilities of LATP electrolyte in lithium batteries lead to the failure, which hinders its further development. Herein, a MoS_2 coating layer as an artificial solid electrolyte interphase (ASEI) is used for modifying the surface of LATP (MCLATP) via an economical and uncomplicated spin coating method, which not only effectively inhibits the decomposition of LATP, but also in-situ forms a conversion layer consisting of Li_2S and Mo metal during cycling. The conversion layer can improve the interfacial charge transfer kinetics and decrease the charge transfer resistance. According to interfacial modification of MoS_2, the symmetric cells show slight polarization, and the Li/MCLATP/LFP cells demonstrate excellent cycling performance over 300 cycles at 1 C. The enhanced batteries performance is ascribed to interfacial modification of MoS_2 as an ASEI layer, which reduces interfacial concentration polarization caused by the formed microcracks around the surface during decomposition of LATP. This work provides a promising strategy to construct the interface between Li metal and solid-state electrolytes for other unstable electrolytes beyond NASICON.

* Corresponding author.
** Corresponding author.
E-mail addresses: yuanshuoguo@cug.edu.cn (S. Yuan), jinhongyun@cug.edu.cn (H. Jin).

https://doi.org/10.1016/j.jpowsour.2022.231491
Received 4 March 2022; Received in revised form 12 April 2022; Accepted 18 April 2022
Available online 26 April 2022

1. Introduction

Lithium-ion batteries (LIBs) are widely used in portable electronic devices and electric vehicles in today's mobile society [1–3]. However, the risk of leak out and explosion in traditional LIBs with liquid electrolytes hinders its development [4]. The severe short circuits caused by the growth of Li dendrite and the capacity fading caused by the failure of the interface in batteries hinder their further applications [5]. The demand for high energy density and high safety promotes the development of solid-state lithium batteries (SSLBs) [6,7].

Solid-state electrolytes (SSEs), as a key component of SSLBs, have been widely studied over the past years [8,9]. Among various SSEs, NASICON-type electrolyte $Li_{1.4}Al_{0.4}Ti_{1.6}(PO_4)_3$ (LATP) with high ionic conductivity ($\sim 10^{-3}$ S cm^{-1}) and low cost is considered as one of the most attractive alternatives to liquid electrolytes [10–12]. Despite the above advantages, the instability against the Li metal anode that widely exists in NASICON-type electrolytes restricts its development [13–15]. Because of the strong reducibility of Li metal anode, it can react with Ti^{4+} of LATP to lower valence, leading to the formation of a high electronic conductive phase like $Li_3Al_{0.3}Ti_{1.7}(PO_4)_3$ [16,17]. Typically, the electronic conductivity of $Li_3Al_{0.3}Ti_{1.7}(PO_4)_3$ is three orders higher than $Li_{1.3}Al_{0.3}Ti_{1.7}(PO_4)_3$, which transforms the interface from ionic conductive to mixed conductive and induces the continuous side reaction. The high electronic conductivity of the interface can accelerate the formation of the interfacial phase and growth of Li dendrite [18–20]. The formation of the interfacial phase brings the volume expansion that generates the local strain in the interface [13,15], leading to the crack formation and the collapse of the SSEs [13,21]. In addition, the bad contact and severe side reaction make the transport of lithium-ion across the interface difficult [22–25]. All of these eventually lead to the failure of batteries.

It is considered an effective way to improve the interface of NASICON-based SSLBs by hindering the transport of electrons and improving the interfacial contact of LIBs [26–28]. Molybdenum disulfide (MoS_2), as a type of transition metal dichalcogenides (TMDCs), has been widely applied in energy storage devices, electronic sensors, and catalysis [29–32]. The poor electronic conductivity makes it suitable for interfacial modification. Cha et al. [33] employed MoS_2 to protect Li metal anode via sputtering and lithiation. The nanoflakes formed during lithiation and the phase of MoS_2 converts from 2H to 1T. It is believed that the 1T-MoS_2 can lower the surface migration energy barrier for Li ion migration along the surface of MoS_2, which explained the stable Li deposition and suppression of dendrite nucleation sites. The Li–S battery with the 3D carbon nanotubes (CNTs)–S cathode (~33 wt% S content) and the MoS_2-coated Li anode exhibit steady cycling for more than 1200 cycles under 0.5C. The different result has been obtained by Yang et al. [34] They adopted MoS_2 modified carbon paper as interlayer materials. They found that MoS_2 would be reduced to Mo and Li_2S during the beginning of Li plating. Moreover, the lowest diffusion energy barrier and highest adsorption energies of Mo make it act as a pre-nucleator to guide uniform Li deposition. The batteries assembled with modified carbon paper show high capacity retention of 78% after 3000 cycles under 2 C. Fu [35] modified the surface of LLZO with MoS_2 by 'polishing' process and the modified LLZO show high critical current density about 2.2 mA cm^{-2} at 100 °C. They think the improvement can attribute to the decomposition product of MoS_2 which can adjust the interfacial reaction. Kizilaslan [36] also applied MoS_2 as artificial solid electrolyte interface (ASEI) materials by spreading the exfoliated 2H–MoS_2 on the surface of Lithium chip in Li–S battery, which shows 13.58% capacity fade after 200 cycles.

Previous studies that use costly deposition method and/or tedious processing technology are not feasible for large-scale applications and the mechanism is needed to further clarify. Herein, we use a simple and low-cost method to propose MoS_2 as ASEI to modify the NASICON-type SSEs, which is effectively to overcome the issues of the interface in electrolytes, achieving enhanced cycle performance at practically high rate. The MoS_2 coating layer is conformally coated on the surface of LATP, which can significantly lower the charge transfer resistance and improve the interfacial ion transport performance. The low charge transfer resistance means faster charge transfer kinetics and low interfacial concentration polarization. What's more, the facile and cost-effectively strategy can also be widely used to various solid electrolytes. This work can be also extended to various TMDCs, which is believed to accelerate the practical application of SSEs in SSLBs.

2. Results and discussions

The LATP pellets are synthesized by solid-state method and the details are shown in the experimental section. The ionic conductivity of LATP under room temperature is 8.73×10^{-4} S cm^{-1} and the activation energy of LATP is 0.27 eV (Fig. S1). The Li^+ transference number is close to 0.99. These results show that the LATP pellets have good electrochemical properties. The MoS_2 layer is fabricated on the surface of LATP via spin coating. With the addition of PVDF, the mixed solution of MoS_2 and n-methyl pyrrolidone (NMP) becomes sticky, making it easier to adhere to the surface of LATP to get a thinner and flatter MoS_2 layer. We can control the thickness of the coating layer by adjusting spin coating speed and viscosity of the mixed solution. The phase information of the LATP pellet, MoS_2 powder and the MoS_2 coated LATP (MCLATP) are analyzed by X-ray diffraction (XRD) (Fig. 1a). The diffraction peaks of the LATP pellet are consistent well with the $LiTi_2(PO_4)_3$ crystallite (PDF# 35–0754). No peak of $AlPO_4$, which is the main impurity phase during the synthesis of LATP, is found [37]. It is attributed to the addition of excess Li which can compensate for Li volatilization during sintering. The phase of MoS_2 raw powder is 2H phase (PDF# 73–1508). After the coating of MoS_2, the peaks of MCLATP agree well with the peaks of 2H–MoS_2 and $LiTi_2(PO_4)_3$. No other peak is found, which means that there is no interaction between MoS_2 and LATP. It can also be attested to the stability of MoS_2 for modifying LATP.

The existing state of MoS_2 before and after the coating is investigated by scanning electron microscopy (SEM), as shown in Fig. 1(b-e). Before coating, MoS_2 powder is in the shape of a sheet. After being mixed with PVDF and spin coating, the distribution of MoS_2 on the surface of LATP is uniform with the shape of the sheet, which matches well with the shape of bulk MoS_2. It indicates that the coating process does not destroy the structure of MoS_2. The addition of PVDF glues the MoS_2 sheets and flatten the surface of LATP, compared with the surface of LATP (Fig. S2). A thin and flattened layer can be found from the cross-section view. The corresponding energy-dispersive spectroscopy (EDS) mapping (Fig. S3) exhibits a uniform distribution of Mo and S elements, conforming the layer is the coating layer. With the assistant of XRD and SEM, the coating layer is revealed to be uniformly distributed on the surface of the LATP pellet with a thickness of about 1.7 μm.

To verify the electrochemical properties of MCLATP, cyclic voltammetry (CV), electrochemical impedance spectrum (EIS), and galvanostatic cycling experiments are carried out. From the CV results of symmetric cell assembled with MCLATP (Fig. S4), the oxidation and reduction peaks of the battery appear at 3.8 V and 2.9 V, which is in accord with the oxidation and reduction peaks of $LiFePO_4$ (LFP) [38]. No other oxidation and reduction peaks are found in the CV results, which prove the electrochemical stability of the MoS_2 coating layer as ASEI.

Galvanostatic charging and discharging cycling experiments are used to investigate the electrochemical stability during stripping and plating. As shown in Fig. 2(a-c), the Li/MCLATP/Li symmetric cell shows a larger overpotential of 0.1 V at the beginning of the cycling at the current density of 0.05 mA cm^{-2} and a capacity of 0.05 mAh cm^{-2}. The overpotential of the Li/LATP/Li symmetric cell is about 0.05 V at the same time. But the cycle continues, the overpotential of Li/LATP/Li cell is up to 1.5 V after 150 cycles when the overpotential of Li/MCLATP/Li only reaches 0.6 V. To investigate the underlying mechanism, the resistance of the symmetric cells before and after cycling is measured by EIS, as shown in Fig. 2d. The equivalent circuit model and fitting results are

shown in Fig. S5 and Table S1. The interfacial resistance of Li/LATP/Li cell is 1101 Ω when the resistance of Li/MCLATP/Li cell is 1911 Ω before cycling. The low interfacial resistance of Li/LATP/Li cell may be attributed to the decomposition of LATP [14]. The formation of the interfacial product can improve the interfacial contact at the initial stage with small interfacial resistance, which is beneficial to lower overpotential. In contrast, because of the lack of Li salt, the coating layer just contains MoS_2 and PVDF and the ionic transport relies on MoS_2 in the coating layer. Thus, the MCLATP has higher interfacial resistance after the addition of the coating layer. The charge transfer resistance of Li/LATP/Li cell is 104.6 Ω, which shows good interfacial ion transport. It can also be attributed to the good interface contact brought by the decomposition of LATP. But the charge transfer resistance of Li/MCLATP/Li cell is 1613 Ω. The bad interfacial ionic conductivity indicates the poor interfacial ion transport, which can explain the high overpotential of Li/MCLATP/Li cell. The high charge transfer resistance may be caused by the poor ionic transport kinetics of MoS_2 coating layer. But the charge transfer resistance rapidly reaches up to 12,605 Ω when the interfacial resistance is 11,605 Ω for Li/LATP/Li cell after cycling. It indicates the failure of the cell, which is further confirmed by the surface photo of the electrolyte after cycling (Fig. S6). The electrolyte pellet is pulverized after cycling. In contrast, the Li/MCLATP/Li cell shows smaller charge transfer resistance of 3677 Ω after the same cycle and the pellet remains in good shape after cycling, which reflects that the decomposition of LATP has been restrained. From the results of EIS, the addition of MoS_2 to the interface can improve the interfacial charge transfer kinetics.

It can be further proved by the curve change of the cycling curve of galvanostatic experiments. The curve type reflects the interfacial charge transfer state and concentration polarization [39]. The arcing voltage curve as shown in Fig. 2e means the large concentration gradients near the interface. The rate-determining step is mass transport at this stage. If the quasi-steady-state concentration profile is quickly reached and the rate-determining step is reaction kinetics, the arcing voltage curve will be short and the curve will reach a plateau quickly. As a consequence, the difference between initial voltage and final voltage can reflect the interfacial charge transfer resistance. The initial and final voltage is extracted from the cycle (Fig. S7) and the ΔE-versus-cycle number curve is shown in Fig. 2f. The initial ΔE of Li/LATP/Li cell is smaller than that of Li/MCLATP/Li cell, indicating that the decomposition improves interfacial contact and charge transfer at the initial stage, which is consistent with the charge transfer resistance. Then, the ΔE of Li/LATP/Li cell continuously increases and the voltage curve changes from flat curve to shape arc curve. It reflects the interface becomes worse and the mass transport across the interface becomes difficult which is also confirmed by the results of EIS. The ΔE of Li/MCLATP/Li cell has a smaller slope, which means the interface keeps steady during cycling and the concentration polarization is also smaller for Li/MCLATP/Li cell. The long-term cycling performance of the symmetric cells at a higher current density is also measured, as shown in Fig. S8. The Li/LATP/Li cells show a small initial polarization voltage at a current density of 0.15 mA cm^{-2}. But the polarization voltage rapidly reaches up to 5 V within 60 h, indicating the severe polarization at the interface under high current density. In contrast, Li/MCLATP/Li cells show slow polarization under the same current density and cycle for more than 300 h, indicating the MoS_2 coating layer effectively improves the stability of the interface. Herein, the galvanostatic cycling and EIS results indicate that the addition of MoS_2 can restrain the decomposition of LATP as other interfacial modified materials. It can also improve the interfacial stability by lowering the charge transfer resistance to lower the interfacial concentration polarization, which is further proved by the SEM results.

The spin coating rate is adjusted to evaluate the influence of the film thickness, as shown in Fig. S9. When the coating rate is 2000 rpm (MCLATP_2000) and 8000 rpm (MCLATP_8000), the thickness of the coating layer is 4.03 μm and 853 nm, respectively. The symmetric cells are assembled to evaluate the electrochemical performance of MCLATP with different thicknesses. The impedance of Li/MCLATP_8000/Li symmetric cells is about 2400 Ω when that of Li/MCLATP_2000/Li symmetric cells is up to 25,000 Ω. The Li/MCLATP_2000/Li symmetric cells only cycle 50 h at a current density of 0.15 mA cm^{-2} with high polarization voltage, which contributes to the high impedance of the cells. But Li/MCLATP_8000/Li symmetric cells last 225 h at the same current density with a smaller initial polarization voltage. There is an evident difference in the shape of the plating and stripping curves. The Li/MCLATP_2000/Li cells show a flat plateau, indicating slight concentration polarization. The Li/MCLATP_8000/Li cells show the same arcing curve as Li/MCLATP/Li cells, which means Li/MCLATP_8000/Li and Li/MCLATP/Li symmetric cells are faced with higher concentration polarization than Li/MCLATP_2000/Li cells. These results indicate that

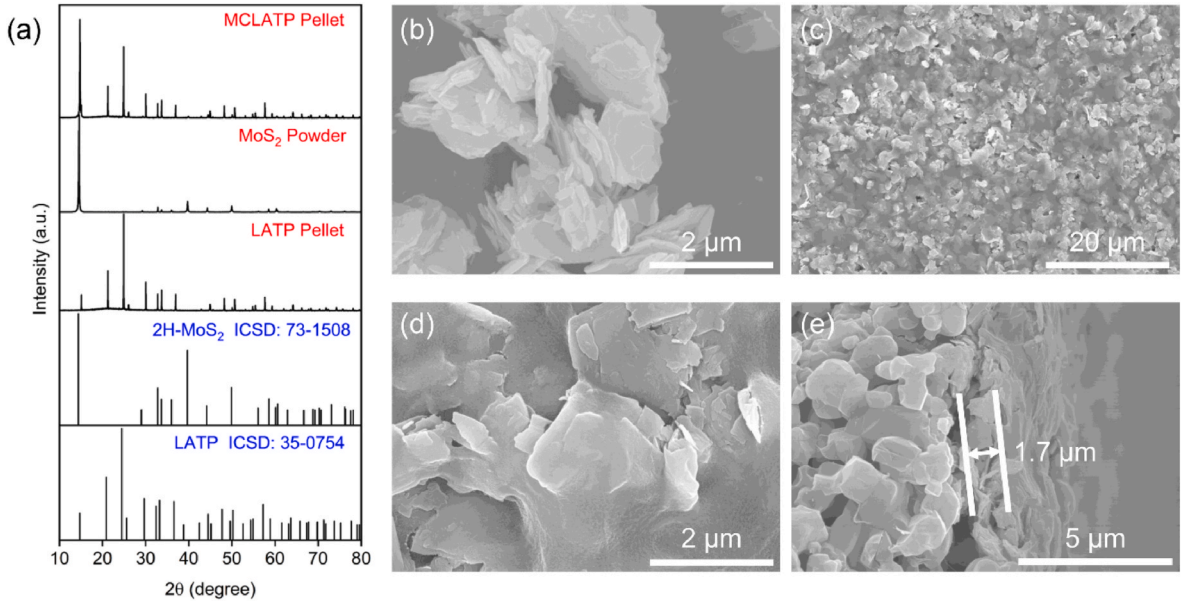

Fig. 1. (a) XRD patterns of LATP pellet, MoS_2 powders and MCLATP pellet, SEM images of (b) MoS_2 powders, (c) surface of MCLATP and (d) larger version, (e) cross-section image of MCLATP.

the coating layer has lower ionic conductivity than LATP and a thicker coating layer brings higher impedance and lower concentration polarization. The coating layer with suitable thickness can inhibit the decomposition of LATP to lower the concentration polarization and has lower impedance to reduce the ohmic polarization.

To demonstrate the feasibility of the coating of MoS_2 in a practical system, Li/LATP/LFP full cells are fabricated for long-term cycling. The cell structure is shown in Fig. 3a, the electrolyte pellet is sandwiched between Li metal anode and cathode plate. Nickel foam and stainless-steel sheet as the current collector of anode and cathode, respectively. 7.5 μL of liquid electrolyte is added to the interface of electrolyte and cathode to get better interfacial contact. Then the batteries are cycled at 1 C under 60 °C. The cycling performances of the batteries assembled with LATP and MCLATP and corresponding charge-discharge profiles are plotted in Fig. 3(b-d). The initial capacity is up to 126.5 mAh g^{-1} for LATP but rapidly fading. The capacity is only 75.3 mAh g^{-1} after 50 cycles and corresponding capacity retention is about 60%. The Li/MCLATP/LFP cell can cycle for more than 300 cycles when reaching the same capacity retention. The Li/MCLATP/LFP cell shows good cycle performance compared to those reported NASICON-type based SSLBs recently in terms of cycle number and C rate listed in Table S2. The good rate performance of Li/MCLATP/Li cell is shown in Fig. 3e and corresponding charge-discharge profiles are shown in Fig. 3f. It delivers the specific discharge capacities of 160.6 mAh g^{-1}, 156.5 mAh g^{-1}, 145.6 mAh g^{-1}, 140.2 mAh g^{-1}, 136.7 mAh g^{-1} at 0.1C, 0.2C, 0.5C, 0.8C and 1 C. The discharge capacity reaches up to 158.8 mAh g^{-1} when it returns to 0.1C, which shows good rate performance. To investigate the effect of the MoS_2 coating layer on the interface resistance, the EIS results of the batteries assembled with LATP and MCLATP are shown in Fig. 3(g-h). The fitting results are shown in Table S3. The interfacial resistance of the batteries assembled with LATP and MCLATP is 14.3 Ω and 8.083 Ω, respectively. The charge transfer resistance of Li/LATP/LFP and Li/MCLATP/LFP cells is 24 Ω and 34.94 Ω. The interfacial resistance and the charge transfer resistance of these two types of batteries show almost no difference and far less than the resistance of symmetric cells. It may be attributed to that the liquid electrolyte added in the interface of electrolyte and cathode can infiltrate into the interface of electrolyte and anode. Therefore, the batteries have small interfacial resistance because of the good interfacial contact with the assistance of liquid electrolyte, which can explain the small polarization of the full cells. To evaluate the effect of liquid electrolyte, the batteries that have the addition of liquid electrolyte on both sides have been assembled, the EIS results of which are shown in Fig. S10. The resistance of the batteries added liquid electrolyte on both sides is about 100 Ω, which is the same as the resistance of the batteries added liquid electrolyte on one side. The Li/liquid electrolyte/LATP/liquid electrolyte/LFP cell can only cycle for 70 cycles with the capacity retention of 60% (Fig. S11). From the results of EIS and long-term cycling of Li/liquid electrolyte/LATP/liquid electrolyte/LFP, the resistance of the full cell is far smaller than the resistance of symmetric cells. Thus, the addition of liquid electrolyte can improve the initial interface contact. But the cycling performance of Li/liquid electrolyte/LATP/liquid electrolyte/LFP is just a little bit better than the cycling performance of Li/LATP/liquid electrolyte/LFP, which indicates that the liquid electrolyte has a slight influence on the cycling stability of full cells. This is further be confirmed by XPS results. The failure of LATP-based batteries mainly contributes to the decomposition of LATP when contact with Li metal anode. From the results of galvanostatic charging and discharging cycling experiments, the coating of MoS_2 can improve the interfacial ion transport and lower the charge transfer resistance. The resistance of batteries after 50 cycles are measured, which is shown in Fig. 3(g-h). The charge transfer resistance of Li/LATP/LFP cell is 1077 Ω when that of Li/MCLATP/LFP cell is 65.07 Ω at the same time. The charge transfer resistance has been significantly reduced with the modification of MoS_2, which is in good consistent with the results of symmetric cells. Therefore, the coating of MoS_2 on the surface of LATP not only separates LATP from contacting with Li metal anode to avoid the decomposition, but also improves the interfacial ion transport by lowering the charge transfer resistance.

The good interface stability of MCLATP is further confirmed by the results of the SEM. The cross-section image shown in Fig. 4a exhibits obvious cracks that appeared in LATP after cycling. The digital photo of the surface of LATP contact with cathode after cycling also shows the cracks, which indicates the decomposition of LATP [13–15]. The region near the surface contact with Li metal anode shows obvious volume expansion. The larger version of this region is shown in Fig. 4b. LATP presents distinct amorphization compared with the pellet before cycling (Fig. S2). And there are large amounts of microcracks distributed over the whole cross-section, which may be caused by the decomposition of LATP and lead to the failure of the interface [40]. Meanwhile, there are lots of cracks distributed over the surface of LATP (Fig. 3c). the

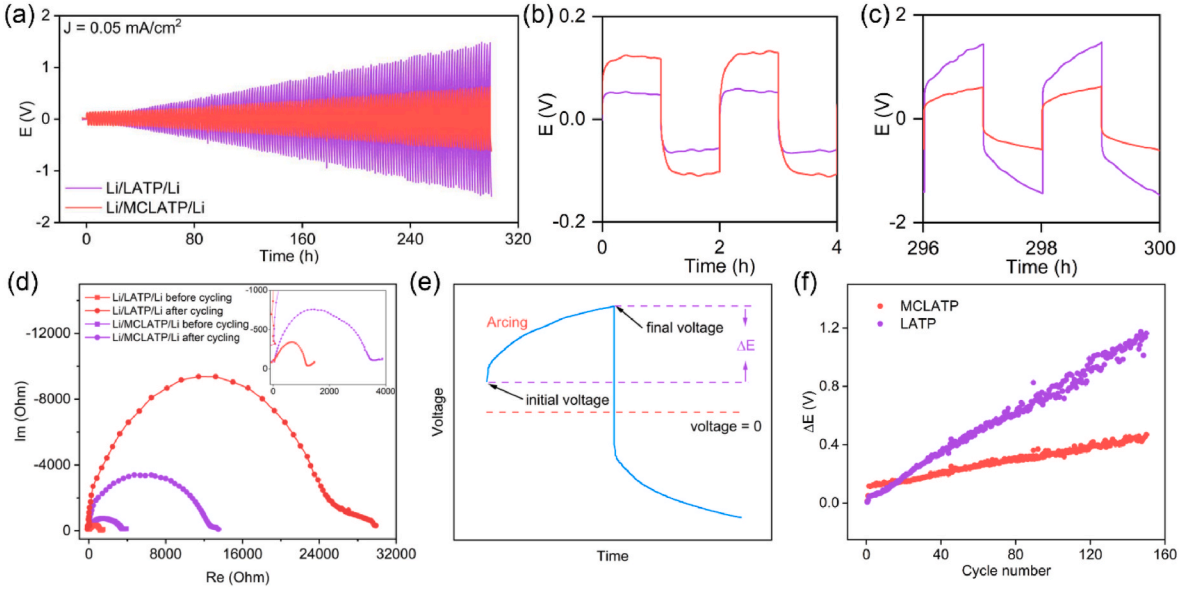

Fig. 2. (a) Plating/stripping profiles of Li/LATP/Li and Li/MCLATP/Li symmetric cells at a current density of 0.05 mA cm^{-2}. Voltage profiles of (b) initial and (c) final cycles, (d) Impedance spectroscopy of Li/LATP/Li and Li/MCLATP/Li symmetric cells before and after cycling. (e) Illustration of arcing voltage curve. (f) ΔE curve over cycle number of Li/LATP/Li and Li/MCLATP/Li symmetric cells.

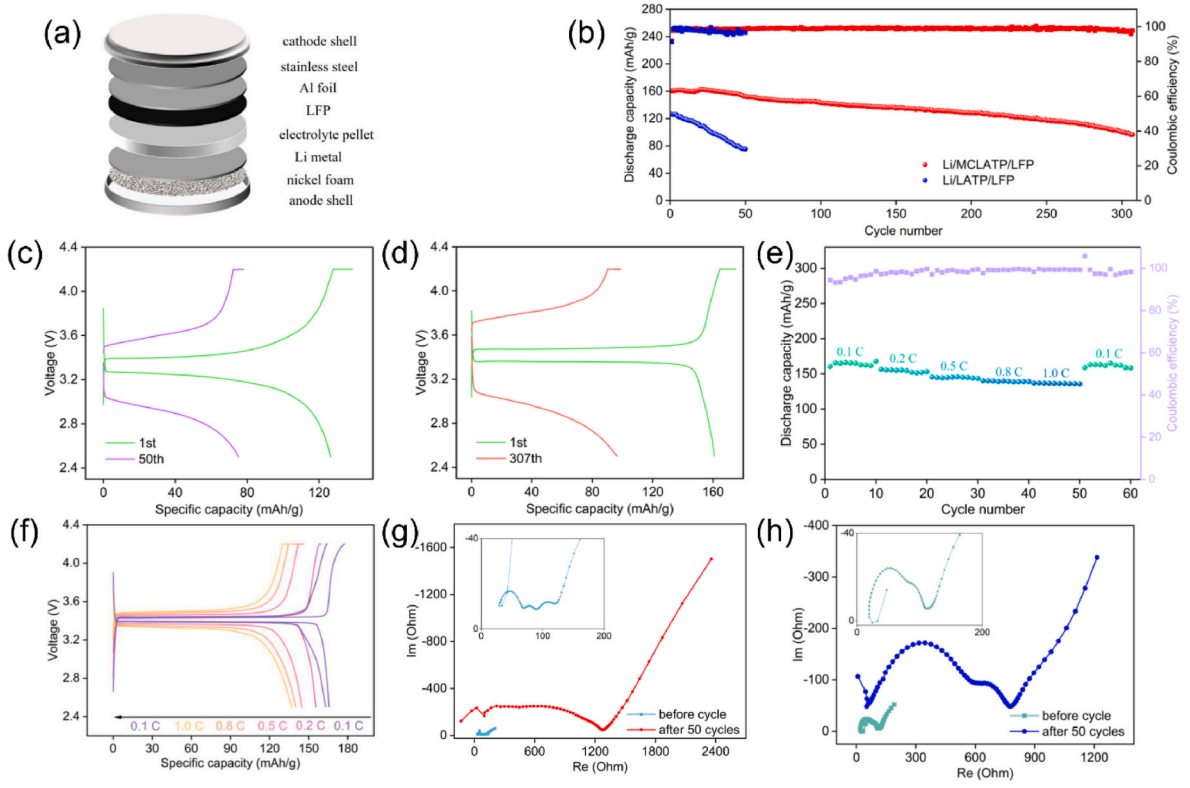

Fig. 3. (a) Schematic of CR2032 coin cell. (b) Long-term cycling test of Li/LATP/LFP and Li/MCLATP/LFP cells at 1 C and (c, d) corresponding charge-discharge profiles. (e) Rate performance of Li/MCLATP/LFP cell tested at various C-rates from 0.1C to 1 C and (f) corresponding charge-discharge profiles. Impedance spectroscopy of (g) Li/LATP/LFP and (h) Li/MCLATP/LFP cells before and after 50 cycles.

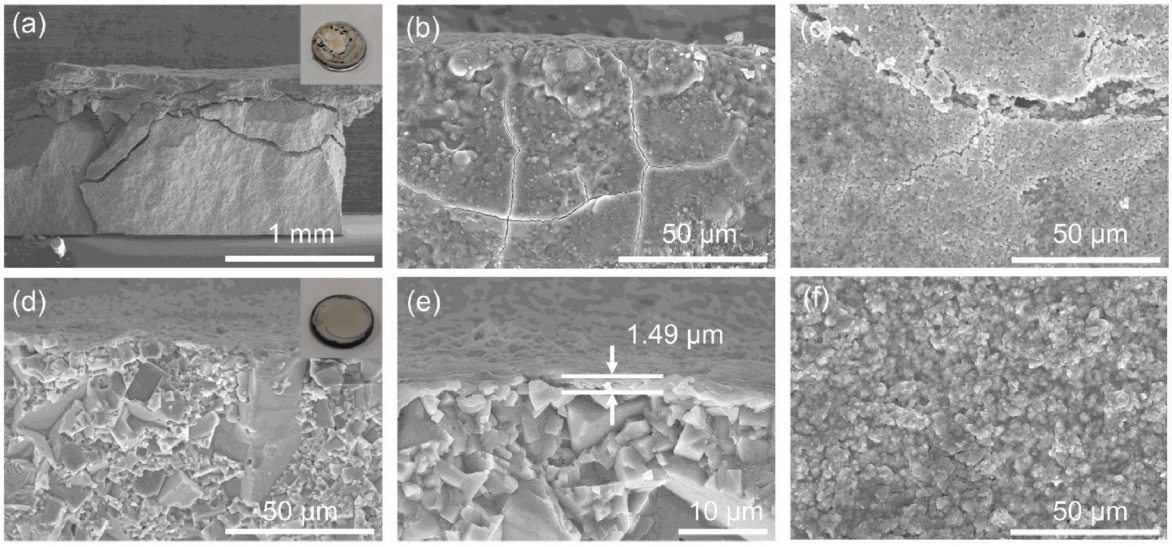

Fig. 4. Cross-section SEM images of (a) Li/LATP/LFP and (d) Li/MCLATP/LFP cells after 50 cycles, the inserts are digital photos of the surface contact with cathode. The larger version of the cross-section images of (b) Li/LATP/LFP and (e) Li/MCLATP/LFP cells after 50 cycles. The surface images of (c) Li/LATP/LFP and (f) Li/MCLATP/LFP cells after 50 cycles.

microcracks distributed near the surface can illustrate the large concentration polarization of LATP symmetric cell. The microcracks caused by the decomposition of LATP impedes ionic mass transport across the interface, leading to the low effective diffusion coefficient that establishes a greater concentration gradient near the interface [39]. Thus the symmetric cell assembled with LATP has large concentration polarization. In contrast, the surface and cross-section of MCLATP after cycling have no cracks (Fig. 4d). The LATP is not reduced by Li metal anode and the pellet remains good crystallinity, which can be attributed to the protection of MoS_2. From the larger version of the cross-section image (Fig. 4e), the coating layer keeps a good shape and good contact with LATP after cycling, which proves the validity of the coating layer. This viewpoint is confirmed by SEM and EDS results of other regions of MCLATP after cycling (Fig. S12). Therefore, the MoS_2 coating layer significantly improves the performance of LATP during cycling. The failure of LATP is in connection with the structural damage and severe

concentration polarization caused by cracks.

To investigate the underlying modification mechanism and the charge of the coating layer during cycling, X-ray photoelectron spectroscopy (XPS) analysis is conducted, as shown in Fig. 5. There is no peak of Ti^{4+} in the Ti 2p spectra (Fig. 5 a) of LATP after cycling, indicating the Ti^{4+} is reduced to Ti^{3+} in LATP during cycling without the protection of MoS_2. The thickness of the modification layer is about 1.49 μm, which is far larger than the typical detection depth of XPS of about several nanometers [41]. There is no peak in the Ti 2p spectra of MCLATP after cycling. It also means the decomposition of LATP has been adequately suppressed. For Li 1s spectra in Fig. 5b, the peak around 56.5 eV and 55.16 eV may correspond to $LiPF_6$ and LiF [42–44], which are found in both LATP and MCLATP samples. It means that the addition of liquid electrolytes in the interface between cathode and electrolyte pellet infiltrate to the anode side. LiF is the decomposition product of $LiPF_6$ during cycling and is the component of SEI. It explains the good interface contact and small charge transfer resistance of full cells, which has been confirmed by the cycle performance of the batteries with the addition of liquid electrolytes on both sides. The peak around 54.60 eV represents Li 1s of Li_2S [45], indicating the reaction of MoS_2 with Li metal.

In the case of Mo 3d in Fig. 5c, there are obvious 2H–MoS_2 (232.24 eV and 229.08 eV) peaks in the spectra of MCLATP before cycling and all peaks correspond well with typical 2H–MoS_2 [46], indicating the stability of MoS_2 with LATP. After cycling, the Mo 3d features can be deconvoluted into four peaks. The peaks at 230.55 eV and 227.50 eV correspond to the Mo $3d_{3/2}$ and $3d_{5/2}$ of Mo metal [35]. The other two peaks at 225.56 eV and 224.43 eV are assigned to the S 2s of 1T-Li_xMoS_2 and Li_2S. It indicates that the 2H–MoS_2 reacts with Li metal and convert to Li_2S and Mo metal. The appearance of 1T-Li_xMoS_2 reflects the phase transition of MoS_2 during lithiation, which is corresponding to the previous reports [33–35]. It is further confirmed by the S 2p spectra. As shown in Fig. 5d, the S 2p spectra also show distinct phase transitions. The peaks lie at 163.10 eV and 161.91 eV represent S $2p_{1/2}$ and $2p_{3/2}$ of 2H–MoS_2. It converts to 1T-Li_xMoS_2 (162.64 eV and 161.56 eV) during cycling, accompanied with the formation of Li_2S (160.98 eV and 159.90 eV).

From the results of SEM and XPS, the modification mechanism of MoS_2 is illustrated in Fig. 6. As for LATP, cracks and collapse of the SSEs occur after cycling, which lead to the failure of the interface, as shown in Fig. 6a. It is accompanied by the formation of microcracks around the surface of LATP contacted with Li metal anode, which lower the effective diffusion coefficient and cause severe concentration polarization. With the modification of MoS_2, as shown in Fig. 6b, the interface remains good contact after cycling. MoS_2 reacts with Li metal and undergo phase transition during cycling. the conversion product, Li_2S and Mo, can accelerate the Li ion transport at the interface [34,35]. It explains the lower charge transfer resistance of MCLATP after cycling. With the improvement of charge transfer kinetics, the concentration gradient around the interface is decreased and the concentration polarization is alleviated. The MCLATP shows a smaller polarization voltage after a long cycle. But the reaction and phase transition of MoS_2 also destroy the coating layer, leading to the shape change of MoS_2 and the crack formation during cycling. It may explain the failure of MCLATP. The performance of the coating layer will be further improved with the process improvement. In a word, MoS_2 shows good potential as an ASEI and is believed to accelerate the practical employment of SSEs in SSLBs.

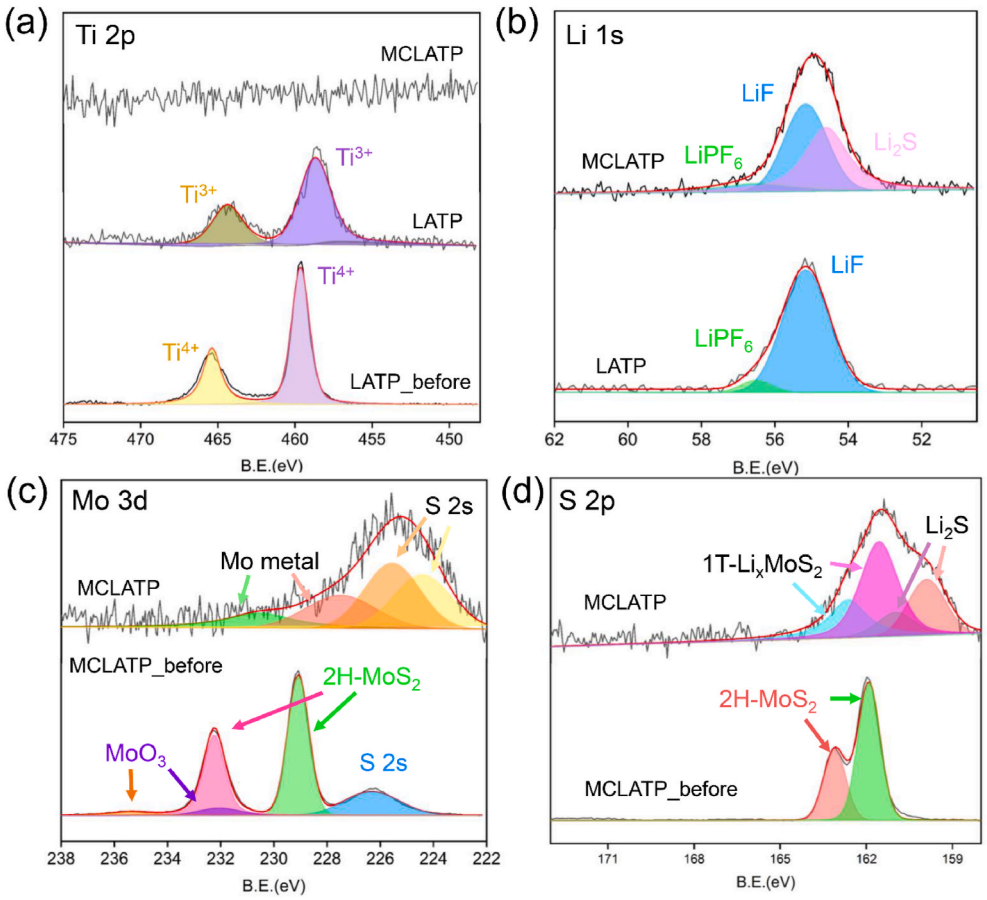

Fig. 5. (a) Ti 2p XPS spectra of LATP, MCLATP after cycling and LATP before cycling. (b) Li 1s XPS spectra of LATP and MCLATP after cycling. (c) Mo 3d and (d) S 2p XPS spectra of MCLATP before and after cycling.

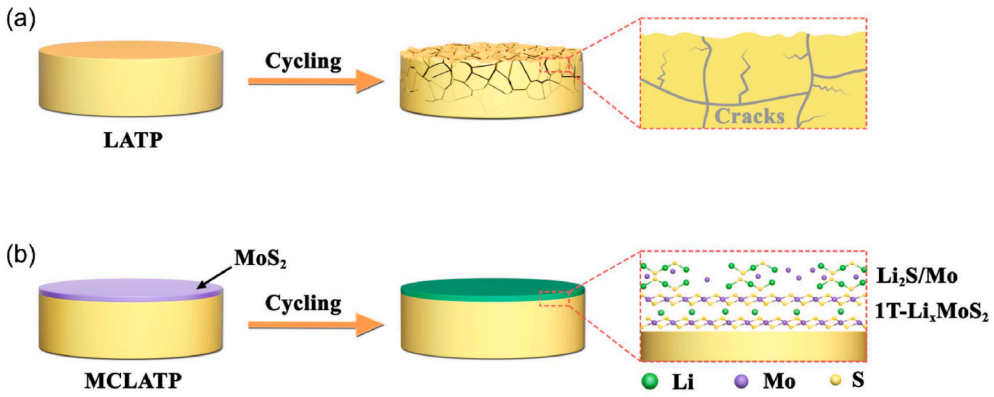

Fig. 6. Schematic illustration of LATP evolution (a) without modification and (b) with modification.

3. Conclusion

In summary, a MoS_2 coating layer as an ASEI is fabricated on the surface of LATP by an economical and uncomplicated spin coating method. According to interfacial modification of MoS_2, the batteries cycle for more than 300 cycles when unmodified batteries just cycle 50 cycles under the same capacity retention. These results reveal that the failure of LATP-based batteries is related to the severe concentration polarization, there are lots of microcracks around the surface contacted with Li metal anode, which decreases the effective diffusion coefficient and leads to bad interfacial mass transport and huge charge transfer resistance. The bad interfacial compatibilities further lead to the failure of the batteries. With the modification of MoS_2, the batteries show smaller charge transfer resistance and polarization. It contributes to the in-situ formed conversion layer consisting of Li_2S and Mo metal during cycling, which not only tune the interfacial mass transport and improve the charge transfer kinetics, but also suppress the decomposition of LATP. This work would broaden the application of SSEs with interfacial modification and facilitate the development of high-performance SSLBs.

4. Experimental

4.1. Electrolytes and cell preparations

$Li_{1.4}Al_{0.4}Ti_{1.6}(PO_4)_3$ (LATP) were prepared by a solid-state method [10]. All chemicals were of analytical grade and purchased from Sinopharm Chemical Reagent Co., Ltd. First, stoichiometric amounts of $NH_4H_2(PO_4)_3$, $LiOH{\cdot}H_2O$, TiO_2, and Al_2O_3 were homogeneously mixed through wet ball-milling in isopropanol. A 5% excess of $LiOH{\cdot}H_2O$ was added. The mixture dried in the oven under 180 °C for 7 days to obtain uniform precursor powders. Then, the precursor powders were calcined in an alumina crucible at 750 °C for 4 h. The powders were subsequently ground by ball-milling in isopropanol again for 10 h. After that, the milled powders were put into a cylindrical pressing mold of 12 mm diameter and pressed under a uniaxial pressure of 200 MPa, followed by sintering at 900 °C for 6 h to form LATP pellets.

The coating of MoS_2 was realized by the spin coating method. The coating solutions were prepared by dissolution of 0.4 g MoS_2 (metal basis, 99.5%, Aladdin) and 0.2 g PVDF in 7 mL NMP (AR, Aladdin). The solution was deposited by spin coating under ambient conditions at 1000 rpm for 20 s and 5000 rpm for 40 s. After that, the pellets dried in a vacuum oven under 70 °C for 12 h.

The cathode was prepared by mixing LFP, carbon black, and PVDF in NMP at a mass ratio of 7: 2: 1 and then coated on an Al foil. After drying at 70 °C in a vacuum oven, the foil was cut into pellets with a diameter of 10 mm. The pellet was further dried at 70 °C in a vacuum oven for 12 h. The areal loading of active materials is about 1 mg cm^{-2}.

After that, CR2032 coin cells were assembled in an argon-filled glovebox (H_2O, O_2 < 0.01 ppm) for electrochemical measurement. The sandwich structure that with the order of foamed nickel, Li metal chip, LATP, LFP, stainless steel sheet was adopted. 7.5 μL of liquid electrolyte (1 M $LiPF_6$ in EC: DMC = 1: 1) was added to the interface of LATP and cathode. Likewise, the symmetric cells were assembled with no addition of liquid electrolyte. After being assembled, the symmetric cells were put in the oven under 100 °C for 2 h to improve the poor interfacial contact.

4.2. Characterization and electrochemical measurement

The structure of LATP and MCLATP were characterized by powder X-ray diffraction (XRD) pattern using a D8-FOCUS X-ray diffractometer with $CuK_{\alpha 1}$ radiation. The morphology and element analysis were acquired by a SU80101 field scanning electron microscope (SEM) and energy dispersive X-ray spectroscopy (EDS). To get the information about the element on the surface of LATP, X-ray photoelectron spectroscopy (XPS) was carried out by Thermo Scientific K-Alpha + using Al Kα X-rays source (1486.6 eV).

All electrochemical impendence spectrum (EIS) was carried by Zennium X electrochemical workstation in the frequency range from 10 MHz to 1 Hz with a 40-mV amplitude. Before the measure of EIS, both sides of LATP were sputtered with Au. CHI760E was carried out to measure cyclic voltammetry (CV) from 2.0 V to 4.5 V with a scan rate of 1 mV/s. The SSLBs and the symmetric cells were conducted on a Wuhan Land battery tester. All of these electrochemical measurements are carried at the temperature of 60 °C.

CRediT authorship contribution statement

Can Huang: Investigation, Conceptualization, Methodology, Writing – original draft, Writing – review & editing. **Zhuojie Li:** Investigation. **Shanshan Duan:** Investigation. **Shuhong Xie:** Supervision, Funding acquisition. **Shuoguo Yuan:** Writing – review & editing, Supervision, Funding acquisition. **Shuen Hou:** Supervision. **Guozhong Cao:** Supervision. **Hongyun Jin:** Writing – review & editing, Supervision, Funding acquisition.

Declaration of competing interest

The authors declare that they have no known competing financial interests or personal relationships that could have appeared to influence the work reported in this paper.

Acknowledgments

This work was financially supported by the National Natural Science Foundation of China (12192213, 51772254), the Key Research and

Development Program of Hubei (2021BAA175), Innovation Team of Hunan Province (2018RS3091), State Key Laboratory of Advanced Technology for Materials Synthesis and Processing (Wuhan University of Technology) (2022-KF-24).

Appendix A. Supplementary data

Supplementary data to this article can be found online at https://doi.org/10.1016/j.jpowsour.2022.231491.

References

[1] J.B. Goodenough, K.S. Park, The Li-ion rechargeable battery: a perspective, J. Am. Chem. Soc. 135 (4) (2013) 1167–1176, https://doi.org/10.1021/ja3091438.

[2] K. Xu, Electrolytes and interphases in Li-ion batteries and beyond, Chem. Rev. 114 (23) (2014) 11503–11618, https://doi.org/10.1021/cr500003w.

[3] C. Yang, Q. Wu, W. Xie, X. Zhang, A. Brozena, J. Zheng, M.N. Garaga, B.H. Ko, Y. Mao, S. He, Y. Gao, P. Wang, M. Tyagi, F. Jiao, R. Briber, P. Albertus, C. Wang, S. Greenbaum, Y.Y. Hu, A. Isogai, M. Winter, K. Xu, Y. Qi, L. Hu, Copper-coordinated cellulose ion conductors for solid-state batteries, Nature 598 (7882) (2021) 590–596, https://doi.org/10.1038/s41586-021-03885-6.

[4] A. Banerjee, X. Wang, C. Fang, E.A. Wu, Y.S. Meng, Interfaces and interphases in all-solid-state batteries with inorganic solid electrolytes, Chem. Rev. 120 (14) (2020) 6878–6933, https://doi.org/10.1021/acs.chemrev.0c00101.

[5] F. Wu, J. Maier, Y. Yu, Guidelines and trends for next-generation rechargeable lithium and lithium-ion batteries, Chem. Soc. Rev. 49 (5) (2020) 1569–1614, https://doi.org/10.1039/c7cs00863e.

[6] Q. Zhao, S. Stalin, C.-Z. Zhao, L.A. Archer, Designing solid-state electrolytes for safe, energy-dense batteries, Nat. Rev. Mater. 5 (3) (2020) 229–252, https://doi.org/10.1038/s41578-019-0165-5.

[7] Y. Xiao, Y. Wang, S.-H. Bo, J.C. Kim, L.J. Miara, G. Ceder, Understanding interface stability in solid-state batteries, Nat. Rev. Mater. 5 (2) (2019) 105–126, https://doi.org/10.1038/s41578-019-0157-5.

[8] C. Wang, K. Fu, S.P. Kammampata, D.W. McOwen, A.J. Samson, L. Zhang, G. T. Hitz, A.M. Nolan, E.D. Wachsman, Y. Mo, V. Thangadurai, L. Hu, Garnet-type solid-state electrolytes: materials, interfaces, and batteries, Chem. Rev. 120 (10) (2020) 4257–4300, https://doi.org/10.1021/acs.chemrev.9b00427.

[9] Y. Shen, Y. Zhang, S. Han, J. Wang, Z. Peng, L. Chen, Unlocking the energy capabilities of lithium metal electrode with solid-state electrolytes, Joule 2 (9) (2018) 1674–1689, https://doi.org/10.1016/j.joule.2018.06.021.

[10] S. Duan, H. Jin, J. Yu, E.N. Esfahani, B. Yang, J. Liu, Y. Ren, Y. Chen, L. Lu, X. Tian, S. Hou, J. Li, Non-equilibrium microstructure of $Li_{1.4}Al_{0.4}Ti_{1.6}(PO_4)_3$ superionic conductor by spark plasma sintering for enhanced ionic conductivity, Nano Energy 51 (2018) 19–25, https://doi.org/10.1016/j.nanoen.2018.06.050.

[11] S.P. Ong, Y. Mo, W.D. Richards, L. Miara, H.S. Lee, G. Ceder, Phase stability, electrochemical stability and ionic conductivity of the $Li_{10\pm1}MP_2X_{12}$(M = Ge, Si, Sn, Al or P, and X = O, S or Se) family of superionic conductors, Energy Environ. Sci. 6 (1) (2013) 148–156, https://doi.org/10.1039/c2ee23355j.

[12] W. Xiao, J. Wang, L. Fan, J. Zhang, X. Li, Recent advances in $Li_{1+x}Al_xTi_{2-x}(PO_4)_3$ solid-state electrolyte for safe lithium batteries, Energy Storage Mater. 19 (2019) 379–400, https://doi.org/10.1016/j.ensm.2018.10.012.

[13] J.A. Lewis, F.J.Q. Cortes, M.G. Boebinger, J. Tippens, T.S. Marchese, N. Kondekar, X. Liu, M. Chi, M.T. McDowell, Interphase morphology between a solid-state electrolyte and lithium controls cell failure, ACS Energy Lett. 4 (2) (2019) 591–599, https://doi.org/10.1021/acsenergylett.9b00093.

[14] H. Chung, B. Kang, Mechanical and thermal failure induced by contact between a $Li_{1.5}Al_{0.5}Ge_{1.5}(PO_4)_3$ solid electrolyte and Li metal in an all solid-state Li cell, Chem. Mater. 29 (20) (2017) 8611–8619, https://doi.org/10.1021/acs.chemmater.7b02301.

[15] J. Tippens, J.C. Miers, A. Afshar, J.A. Lewis, F.J.Q. Cortes, H. Qiao, T.S. Marchese, C.V. Di Leo, C. Saldana, M.T. McDowell, Visualizing chemomechanical degradation of a solid-state battery electrolyte, ACS Energy Lett. 4 (6) (2019) 1475–1483, https://doi.org/10.1021/acsenergylett.9b00816.

[16] J. Zhu, J. Zhao, Y. Xiang, M. Lin, H. Wang, B. Zheng, H. He, Q. Wu, J.Y. Huang, Y. Yang, Chemomechanical failure mechanism study in NASICON-type $Li_{1.3}Al_{0.3}Ti_{1.7}(PO_4)_3$ solid-state lithium batteries, Chem. Mater. 32 (12) (2020) 4998–5008, https://doi.org/10.1021/acs.chemmater.9b05295.

[17] P. Hartmann, T. Leichtweiss, M.R. Busche, M. Schneider, M. Reich, J. Sann, P. Adelhelm, J. Janek, Degradation of NASICON-type materials in contact with lithium metal: formation of mixed conducting interphases (MCI) on solid electrolytes, J. Phys. Chem. C 117 (41) (2013) 21064–21074, https://doi.org/10.1021/jp4051275.

[18] X.-B. Cheng, C. Yan, X.-Q. Zhang, H. Liu, Q. Zhang, Electronic and ionic channels in working interfaces of lithium metal anodes, ACS Energy Lett. 3 (7) (2018) 1564–1570, https://doi.org/10.1021/acsenergylett.8b00526.

[19] H. Liu, X.-B. Cheng, J.-Q. Huang, H. Yuan, Y. Lu, C. Yan, G.-L. Zhu, R. Xu, C.-Z. Zhao, L.-P. Hou, C. He, S. Kaskel, Q. Zhang, Controlling dendrite growth in solid-state electrolytes, ACS Energy Lett. 5 (3) (2020) 833–843, https://doi.org/10.1021/acsenergylett.9b02660.

[20] R. Xu, X.-B. Cheng, C. Yan, X.-Q. Zhang, Y. Xiao, C.-Z. Zhao, J.-Q. Huang, Q. Zhang, Artificial interphases for highly stable lithium metal anode, Matter 1 (2) (2019) 317–344, https://doi.org/10.1016/j.matt.2019.05.016.

[21] L. He, J.A.S. Oh, K. Watarai, M. Morita, Y. Zhao, Q. Sun, T. Sakamoto, L. Lu, S. Adams, Electromechanical failure of NASICON-type solid-state electrolyte-based all-solid-state Li-ion batteries, Chem. Mater. 33 (17) (2021) 6841–6852, https://doi.org/10.1021/acs.chemmater.1c01564.

[22] Z. Gao, H. Sun, L. Fu, F. Ye, Y. Zhang, W. Luo, Y. Huang, Promises, challenges, and recent progress of inorganic solid-state electrolytes for all-solid-state lithium batteries, Adv. Mater. 30 (17) (2018) 1715702, https://doi.org/10.1002/adma.201705702.

[23] X. Han, Y. Gong, K.K. Fu, X. He, G.T. Hitz, J. Dai, A. Pearse, B. Liu, H. Wang, G. Rubloff, Y. Mo, V. Thangadurai, E.D. Wachsman, L. Hu, Negating interfacial impedance in garnet-based solid-state Li metal batteries, Nat. Mater. 16 (5) (2017) 572–579, https://doi.org/10.1038/nmat4821.

[24] W. Zhao, J. Yi, P. He, H. Zhou, Solid-state electrolytes for lithium-ion batteries: fundamentals, challenges and perspectives, Electrochem. Energy Rev. 2 (4) (2019) 574–605, https://doi.org/10.1007/s41918-019-00048-0.

[25] T. Deng, L. Cao, X. He, A.-M. Li, D. Li, J. Xu, S. Liu, P. Bai, T. Jin, L. Ma, M. A. Schroeder, X. Fan, C. Wang, In situ formation of polymer-inorganic solid-electrolyte interphase for stable polymeric solid-state lithium-metal batteries, Inside Chem. 7 (11) (2021) 3052–3068, https://doi.org/10.1016/j.chempr.2021.06.019.

[26] C. Yan, X.-Q. Zhang, J.-Q. Huang, Q. Liu, Q. Zhang, Lithium-anode protection in lithium–sulfur batteries, Trends Chem 1 (7) (2019) 693–704, https://doi.org/10.1016/j.trechm.2019.06.007.

[27] P. Gorai, T. Famprikis, B. Singh, V. Stevanović, P. Canepa, Devil is in the defects: electronic conductivity in solid electrolytes, Chem. Mater. 33 (18) (2021) 7484–7498, https://doi.org/10.1021/acs.chemmater.1c02345.

[28] M. Sun, T. Liu, Y. Yuan, M. Ling, N. Xu, Y. Liu, L. Yan, H. Li, C. Liu, Y. Lu, Y. Shi, Y. He, Y. Guo, X. Tao, C. Liang, J. Lu, Visualizing lithium dendrite formation within solid-state electrolytes, ACS Energy Lett. 6 (2) (2021) 451–458, https://doi.org/10.1021/acsenergylett.0c02314.

[29] T. Wang, S. Chen, H. Pang, H. Xue, Y. Yu, MoS_2-based nanocomposites for electrochemical energy storage, Adv. Sci. 4 (2) (2017) 1600289, https://doi.org/10.1002/advs.201600289.

[30] J. Huang, Z. Wei, J. Liao, W. Ni, C. Wang, J. Ma, Molybdenum and tungsten chalcogenides for lithium/sodium-ion batteries: beyond MoS_2, J. Energy Chem. 33 (2019) 100–124, https://doi.org/10.1016/j.jechem.2018.09.001.

[31] M. Jana, R. Xu, X.-B. Cheng, J.S. Yeon, J.M. Park, J.-Q. Huang, Q. Zhang, H.S. Park, Rational design of two-dimensional nanomaterials for lithium–sulfur batteries, Energy Environ. Sci. 13 (4) (2020) 1049–1075, https://doi.org/10.1039/c9ee02049g.

[32] C.N.R. Rao, K. Gopalakrishnan, U. Maitra, Comparative study of potential applications of graphene, MoS_2, and other two-dimensional materials in energy devices, sensors, and related areas, ACS Appl. Mater. Interfaces 7 (15) (2015) 7809–7832, https://doi.org/10.1021/am509096x.

[33] E. Cha, M.D. Patel, J. Park, J. Hwang, V. Prasad, K. Cho, W. Choi, 2D MoS_2 as an efficient protective layer for lithium metal anodes in high-performance Li-S batteries, Nat. Nanotechnol. 13 (4) (2018) 337–344, https://doi.org/10.1038/s41565-018-0061-y.

[34] X. Yang, X. Gao, S. Mukherjee, K. Doyle-Davis, J. Fu, W. Li, Q. Sun, F. Zhao, M. Jiang, Y. Hu, H. Huang, L. Zhang, S. Lu, R. Li, T.K. Sham, C.V. Singh, X. Sun, Phase evolution of a prenucleator for fast Li nucleation in all-solid-state lithium batteries, Adv. Energy Mater. 10 (37) (2020) 2001191, https://doi.org/10.1002/aenm.202001191.

[35] J. Fu, P. Yu, N. Zhang, G. Ren, S. Zheng, W. Huang, X. Long, H. Li, X. Liu, In situ formation of a bifunctional interlayer enabled by a conversion reaction to initiatively prevent lithium dendrites in a garnet solid electrolyte, Energy Environ. Sci. 12 (4) (2019) 1404–1412, https://doi.org/10.1039/c8ee03390k.

[36] A. Kızılaslan, T. Çetinkaya, H. Akbulut, 2H-MoS_2 as an artificial solid electrolyte interface in all-solid-state lithium–sulfur batteries, Adv. Mater. Interfac. 7 (20) (2020) 2001020, https://doi.org/10.1002/admi.202001020.

[37] H. Chen, H. Tao, Q. Wu, X. Zhao, J. Stevenson, Crystallization kinetics of superionic conductive Al(B,La)- incorporated $LiTi_2(PO_4)_3$ glass-ceramics, J. Am. Ceram. Soc. 96 (3) (2013) 801–805, https://doi.org/10.1111/jace.12094.

[38] D. Yu, C. Fietzek, W. Weydanz, K. Donoue, T. Inoue, H. Kurokawa, S. Fujitani, Study of $LiFePO_4$ by cyclic voltammetry, J. Electrochem. Soc. 154 (4) (2007) A253–A257.

[39] K.-H. Chen, K.N. Wood, E. Kazyak, W.S. LePage, A.L. Davis, A.J. Sanchez, N. P. Dasgupta, Dead lithium: mass transport effects on voltage, capacity, and failure of lithium metal anodes, J. Mater. Chem. 5 (23) (2017) 11671–11681, https://doi.org/10.1039/c7ta00371d.

[40] L. He, Q. Sun, C. Chen, J.A.S. Oh, J. Sun, M. Li, W. Tu, H. Zhou, K. Zeng, L. Lu, Failure mechanism and interface engineering for NASICON-structured all-solid-state lithium metal batteries, ACS Appl. Mater. Interfaces 11 (23) (2019) 20895–20904, https://doi.org/10.1021/acsami.9b05516.

[41] R. Escobar Galindo, R. Gago, D. Duday, C. Palacio, Towards nanometric resolution in multilayer depth profiling: a comparative study of RBS, SIMS, XPS and GDOES, Anal. Bioanal. Chem. 396 (8) (2010) 2725–2740, https://doi.org/10.1007/s00216-009-3339-y.

[42] B.S. Parimalam, A.D. MacIntosh, R. Kadam, B.L. Lucht, Decomposition reactions of anode solid electrolyte interphase (SEI) components with $LiPF_6$, J. Phys. Chem. C 121 (41) (2017) 22733–22738, https://doi.org/10.1021/acs.jpcc.7b08433.

[43] B.S. Parimalam, B.L. Lucht, Reduction reactions of electrolyte salts for lithium ion batteries: $LiPF_6$, $LiBF_4$, LiDFOB, LiBOB, and LiTFSI, J. Electrochem. Soc. 165 (2) (2018) A251–A255, https://doi.org/10.1149/2.0901802jes.

[44] T. Kawamura, S. Okada, J.-i. Yamaki, Decomposition reaction of $LiPF_6$-based electrolytes for lithium ion cells, J. Power Sources 156 (2) (2006) 547–554, https://doi.org/10.1016/j.jpowsour.2005.05.084.
[45] Y. Peng, Y. Zhang, Z. Wen, Y. Wang, Z. Chen, B.-J. Hwang, J. Zhao, Constructing fast electron and ion conductive framework for Li_2S as advanced lithium sulfur battery, Chem. Eng. J. 346 (2018) 57–64, https://doi.org/10.1016/j.cej.2018.04.049.
[46] Y. Yu, Y. Ye, M. Wei, W. Sun, Q. Tang, J. Zhang, X. Chen, H. Li, J. Xu, Three-dimensional MoS_2/rGO foams as efficient sulfur hosts for high-performance lithium-sulfur batteries, Chem. Eng. J. 355 (2019) 671–678, https://doi.org/10.1016/j.cej.2018.08.176.